The Astronomical Journal, 166:216 (9pp), 2023 December https://doi.org/10.3847/1538-3881/ad01ba

A Rotating Accretion Disk around MWC 297, a Young B1.5Ve Star

Göran Sandell[1] and William Vacca[2,3]
[1] Institute for Astronomy, University of Hawai'i at Manoa, Hilo, 640 N. Aohoku Place, Hilo, HI 96720, USA; gsandell@hawaii.edu
[2] NSF's NOIRLab, 950 N. Cherry Avenue, Tucson, AZ 85719, USA; bill.vacca@noirlab.edu
Received 2022 March 28; revised 2023 October 6; accepted 2023 October 8; published 2023 November 2

Abstract

High-resolution spectra with iSHELL on IRTF in the *K* and *M* bands of the young, heavily accreting B1.5Ve star MWC 297 show numerous double-peaked CO lines. These CO lines originate in an inclined gaseous disk in Keplerian rotation. MWC 297 is the only early B star known to show a Keplerian disk in CO. Analysis of the spectra shows that ^{12}CO 1–0 is optically thick for the low excitation lines. Even the ^{13}CO 1–0 and ^{12}CO 2–1 have somewhat optically thick lines at low *J* levels. We find that the CO emission in the disk can be fitted with CO being in a narrow ring at a radius of 12 au, with a temperature of 1500 K and a CO column density of 1.6×10^{18} cm^{-2}. This model underestimates the line strength of high-*J* lines, indicating that they are excited by fluorescence. The CO overtone lines have a similar temperature. The ^{13}CO lines are much brighter than expected from interstellar isotope ratios. The ^{13}CO lines are wider than the ^{12}CO ones, suggesting different excitation conditions. The same is true for ^{12}CO 2–1. We see strong absorption in ^{12}CO and ^{13}CO 1–0 at low *J* levels, which is due to two cold foreground clouds. These clouds, one with a temperature of 8.3 K and a column density of 6.7 10^{17} cm^{-2} and the other one colder and with lower column density, can fully account for the observed extinction toward MWC 297.

Unified Astronomy Thesaurus concepts: Star formation (1569); Star forming regions (1565); Massive stars (732); Circumstellar disks (235); Far infrared astronomy (529)

1. Introduction

Most young, low-mass stars are surrounded by circumstellar disks. The same is also true for intermediate-mass stars up to a spectral type of ∼B8 (Williams & Cieza 2011). Direct detections of disks around early B or O stars are rare. This does not mean that high-mass stars do not have accretion disks; rather, it indicates that disks are much more short-lived around high-mass stars, so that by the time these stars become optically visible they have already dispersed their accretion disks. Furthermore, high-mass stars are generally more distant than low-mass stars, making it harder to spatially resolve their accretion disks. Even O stars with stellar masses of 20–30 $M_\odot$ appear to have disks in their heavy accretion phase (see, e.g., Ilee et al. 2013; Beltrán & de Wit 2016; Zapata et al. 2019; Sandell et al. 2020; Moscadelli et al. 2021). However, such stars are difficult to study because they are always in clusters and deeply embedded.

Most of the evidence for disks around high-mass stars comes from deeply embedded young objects observed with interferometric means, mostly in the millimeter/submillimeter regime with the Atacama Large Millimeter/submillimeter Array (ALMA) and NOEMA and other array telescopes. There are also some detections at optical/infrared wavelengths (Beltrán & de Wit 2016). There has been some success in looking for Keplerian rotation in accretion disks using the rovibrational CO lines at 2.3 μm and at 4.5–5.2 μm. CO overtone emission ($\upsilon = 2$–0 and $\upsilon = 3$–1) was first detected in the BN object (mass $\sim 10\,M_\odot$; Scoville et al. 1979) and in the early B star MWC 349 A (Kraus et al. 2000). The latter has a mass of $\sim 30\,M_\odot$, although recently Kraus et al. (2020) argue that it is a B[e] supergiant. There have been a number of detections of bandhead emission toward massive young stellar objects (Ishii et al. 2001; Blum et al. 2004; Bik & Thi 2004; Bik et al. 2006; Wheelwright et al. 2010; Cooper et al. 2013; Ilee et al. 2013; Pomohaci et al. 2017). For these objects the stellar mass is usually deduced from the observed bolometric luminosity. These can be highly uncertain because it includes emission from the accretion process and possible emission from nearby objects, resulting in an overestimate of stellar mass; see, e.g., W33A, for which Pomohaci et al. (2017) determine a mass of $17.2\,M_\odot$, while Navarete et al. (2021) find a mass of $10\,M_\odot$. Yet it is clear that some of these are indeed very young high-mass stars. The CO fundamental ($\upsilon =$ 1–0) rovibrational lines, located in the *M* band, 4.5–5.2 μm, have been detected in low-mass stars (Najita et al. 2003), HAEBE stars, and transitional disks objects (Brittain et al. 2003; Blake & Boogert 2004; Salyk et al. 2009; van der Plas et al. 2015; Doppmann et al. 2017; Banzatti et al. 2022), but not in high-mass stars ($M > 8\,M_\odot$), except for MWC 297, the subject of this study.

MWC 297 is a bright, nearby HAeBe star with a spectral type B1.5Ve (Drew et al. 1997) and a mass of $\sim 10\,M_\odot$, located at a distance of 418 pc (Gaia DR3; Riello et al. 2021). It has been the subject of several studies with ESO's Very Large Telescope Interferometer (VLTI; Acke et al. 2008; Weigelt et al. 2011; Lazareff et al. 2017; Kluska et al. 2020). Most of these studies suggest that the star is surrounded by an almost face-on disk. The star, however, drives an ionized outflow, with spatially separated outflow lobes, and therefore cannot be face-on (Sandell et al. 2011). Mid-infrared imaging with FORCAST on SOFIA (Vacca & Sandell 2022) shows that hot dust traces the outflow lobes at wavelengths > 20 μm. Simple geometrical modeling of the mid-infrared morphology constrains the disk inclination rather well and gives an inclination angle $i = 55°$.

[3] Visiting Astronomer at the Infrared Telescope Facility, which is operated by the University of Hawaii under contract 80HQTR19D0030 with the National Aeronautics and Space Administration.

Here we present and discuss high-resolution *M*-band data obtained with the iSHELL instrument at the IRTF. The spectrum reveals double-peaked CO emission lines, which we have modeled with a rotating Keplerian disk to determine the properties of the emission region. We also discuss and analyze the absorption spectra from the cold foreground cloud, which are seen in low $\upsilon = 1$–0 *P* and *R* transitions. We note that MWC 297 was included in a large survey of planet-forming disks observed with the same instrument and the same wavelength range, and these data have recently been published (Banzatti et al. 2022). While Banzatti et al. (2022) did classify the double-peaked CO profiles in MWC 297 as originating in a Keplerian accretion disk, they provide very few details. Here we present a more comprehensive analysis of both CO overtone emission at 2.3 μm and the rovibrational spectra in the *M* band.

2. ISHELL Observations and Data Reduction

Observations of MWC 297 were obtained at the NASA Infrared Telescope Facility (IRTF) on Maunakea on 2020 September 30 (UT) and on 2022 April 26 (UT) with iSHELL, the facility near-infrared high resolution cross-dispersed spectrograph (Rayner et al. 2022). The *M*-band observations used the M1 setting of iSHELL in both 2020 and 2022. This mode yields spectra spanning the wavelength range 4.5–5.2 μm over 16 spectral orders. The observations were acquired in "pair mode," in which the object was observed at two separate positions along the 15″-long slit. The slit width was set to 0.″375, which yields a nominal resolving power of 88,000 for the spectra. (At the distance of MWC 297 of 418 pc, the iSHELL 0.″375 slit spans ∼160 au.) Twenty individual exposures of MWC 297, each lasting 28 s, were obtained using the M1 setting of iSHELL. In 2020 the slit was set to the parallactic angle (46.°0) during the observations. In 2022 the observations were done using two slit positions, 197° and 17°, which were coadded in the post reduction. The observations both times were acquired in "pair mode," in which the object was observed at two separate positions along the 15″-long slit. The slit width was set to 0.″375, which yields a nominal resolving power of 88,000 for the spectra. At the distance of MWC 297, 418 pc, the iSHELL 0.″375 slit spans ∼160 au. Long observations of an A0V star, used as a "telluric standard" to correct for absorption due to the Earth's atmosphere and to flux-calibrate the target spectra, were obtained immediately prior to the observations of MWC 297. In 2022 we also observed MWC 297 in the *K* band. These observations were done in the K3 setting, providing a spectral coverage from 2.256 to 2.55 μm. A set of internal flat fields and arc frames were obtained immediately after the observations of MWC 297 for flat-fielding and wavelength calibration purposes.

The data were reduced using Spextool (Cushing et al. 2004), the IDL-based package developed for the reduction of SpeX and iSHELL data. The Spextool package performs nonlinearity corrections, flat-fielding, image pair subtraction, aperture definition, optimal extraction, and wavelength calibration. The sets of spectra resulting from the individual exposures were median-combined and then corrected for telluric absorption and flux-calibrated using the extracted A0V telluric standard spectra and the technique and software described by Vacca et al. (2003). The spectra from the individual orders were then spliced together by matching the flux levels in the overlapping wavelength regions, and regions of poor atmospheric transmission were removed. However, for the 2020 September observations the final M spectrum of the A0V star had relatively poor signal-to-noise ratio (S/N; on the order of 30), and this limited the final S/N of the spectrum of MWC 297, which is considerably brighter in the *M* band. (The reduced spectrum of MWC 297 has an S/N of several hundred.) Therefore, an alternate telluric correction was derived using the *xtellcor_model* software developed by A. Boogert (2022, private communication) and then applied to the reduced spectrum of MWC 297. Although this was effective at correcting the telluric absorption, the resulting spectrum was still uncalibrated. Therefore, we fit a polynomial to the continuum of both the A0V-corrected spectrum and the model-corrected spectrum and multiplied the model-corrected spectrum by the wavelength-dependent ratio of the polynomials. This yielded a telluric-corrected and flux-calibrated spectrum of MWC 297. The S/N varies across the spectrum but is on the order of several hundred across the entire M1 wavelength range. For the 2022 data we used a brighter A0V star, which could directly be used for flux calibration. Direct comparison of the two calibrated data sets shows that the calibration agrees within 10% for both data sets, and we have therefore added together the two data sets, after correcting both spectra for Doppler shifts due to the relative motion of Earth and the source, and extracted flux densities for all lines not affected by telluric absorption. In 2020 the Doppler shift for MWC 297 was –11.5 km s^{-1}, which severely affected CO lines with *J* values $\lesssim 15$, while it was +41.2 km s^{-1}in 2022, which largely shifted all CO lines away from telluric absorption features.

3. A Short Overview of What Has Been Learned from Studies of Rovibrational CO

CO vibrational overtone emission was first detected in the inner disks of both high- and low-mass objects, but it is not as ubiquitous as the CO fundamental ($\Delta\upsilon = 1$) transitions of CO at 4.6 μm. The detection rate of overtone emission in unbiased surveys is about 25%. In part this is due to the relatively low *A*-values, which require high column densities of hot gas for the lines to be detectable, but other factors play a role as well. Modeling by Ilee et al. (2018) suggests that moderate accretion rates produce the most prominent and hence detectable CO first-overtone emission. If the accretion rate is too high ($\gtrsim 10^{-4}\,M_\odot\,\mathrm{yr}^{-1}$), it results in large dust sublimation radii, a larger contribution of hot dust to the *K*-band continuum, and therefore a lower CO-to-continuum ratio. Low accretion rates ($\lesssim 10^{-6}\,M_\odot\,\mathrm{yr}^{-1}$), however, result in smaller dust sublimation radii, a smaller CO-emitting area, and therefore a lower CO-to-continuum ratio. Although CO overtone emission is detectable in MWC 297, which has an accretion rate of $3 \times 10^{-4}\,M_\odot\,\mathrm{yr}^{-1}$, the first-overtone bandhead is barely visible in high-resolution spectra, suggesting that the gas is relatively cold, or about 1000 K. The line profiles of individual transitions are double-peaked. This will be discussed later in the paper.

The rovibrational CO line emission at 4.5–5.2 μm is, as already mentioned, much more ubiquitous and seen in a variety of objects, ranging from transition objects to classical T Tauri and HAEBE stars, but, contrary to CO overtone emission, it is not seen in high-mass stars except for MWC 297 (Banzatti et al. 2022; this paper) and perhaps in BN (Scoville et al. 1983). Banzatti et al. (2022) gives an up-to-date list of all the high-resolution *K*- and *M*-band CO surveys done over the past 20 yr.

Therefore, there is no reason for us to repeat it here. Instead, we try to summarize the major findings resulting from these studies and complementary theoretical modeling.

The rovibrational CO emission at 4.7 μm is very common in protoplanetary disks and arises in the inner 0.1–2 au region in disks around low-mass stars (Najita et al. 2007) and up to 30 au or more in HAEBE stars (van der Plas et al. 2015; Banzatti et al. 2018, 2022). The line shapes vary (Bast et al. 2011; Brown et al. 2013; Banzatti & Pontoppidan 2015; Banzatti et al. 2022). They can be narrow and single-peaked, narrow with a broad pedestal, broad but single-peaked, or pure double-peaked Keplerian profiles. Some stars also show the CO in absorption, which in most cases originates from colder foreground gas. Double-peaked profiles, which are expected to be a true disk signature, are surprisingly uncommon (Bast et al. 2011), although in the large survey by Banzatti et al. (2022) the detection rate of double-peaked lines was quite common, $\sim$ 50%.

Banzatti et al. (2022) define the line profiles in two broad groups depending on line shape: triangular and double-peaked lines. In their classification the single-peaked narrow lines with a broad pedestal and the broad but single-peaked lines all fall into this category. These lines are often somewhat asymmetric, with the blueshifted side being stronger (Herczeg et al. 2011; Brown et al. 2013). Banzatti et al. (2022) define a line shape parameter S as $S =$ FW10%/FW75%, where FW stands for full width at 10% and 75%, respectively. Lines with a shape value $\gtrsim$2.5 are triangular, and those with a shape value of $\lesssim$2.5 are generally double-peaked Keplerian or narrow single-peaked lines. The latter are believed to represent Keplerian disk emission seen in face-on disks. The single-peaked narrow lines with a broad pedestal, i.e., triangular-shaped lines, cannot be explained by Keplerian motion. The broad pedestal may still be Keplerian, but the narrow component appears to originate in a slow-mowing disk wind (Bast et al. 2011; Brown et al. 2013). Pontoppidan et al. (2011) found from spectroastrometry of a narrow line with a broad pedestal that the narrow-line emission is too compact and asymmetric to originate in a Keplerian disk. The broad single-peaked lines are also believed to be a combination of a Keplerian disk rotation and a disk wind, but the disks are seen with higher inclination angles, producing broader lines (Brown et al. 2013).

Line shape alone does not really discriminate where the CO lines are formed, whether they originate from the disk, the outflow, or both. Spectroastrometry (Pontoppidan et al. 2011; Brittain et al. 2018) can achieve subarcsecond resolution and hence put spatial constraints on the emitting region, which has been used to discriminate between Keplerian and wind models. Another powerful constraint is the strength of higher vibrational levels, which have been detected up to $\upsilon = 6$–5 in HAEBE stars (Brittain et al. 2007; Jensen et al. 2021; Banzatti et al. 2022). For double-peaked lines, the work by Banzatti et al. (2018, 2022) and Bosman et al. (2019) suggests that one can identify three emitting regions that show a dependence on the $\upsilon 2/\upsilon 1$ ratio depending on the location of their emitting radii, $R_{\rm CO}$, compared to their dust sublimation radius, $R_{\rm subl}$. Regions 1a and 1b both have high vibrational ratio $\upsilon 2/\upsilon 1 = 0.2$–1.0 but come from very different regions in the disk, although both are largely dust free. Region 1a is inside $R_{\rm subl}$, while 1b is inside a dust cavity observed by millimeter interferometry. Region 1b therefore has lower rotational temperatures and narrower line widths, and it appears that UV fluorescence largely excites the higher vibrational levels in this region (Bosman et al. 2019). In region 2 the vibrational ratio $\upsilon 2/\upsilon 1 = 0.01$–0.2, and the CO is emitted from regions outside the dust rim.

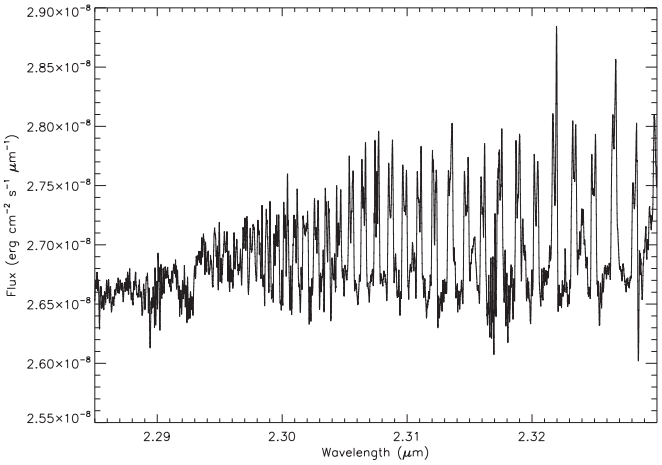

Figure 1. The CO overtone bands observed with iSHELL in *K* band showing a large number of double-peaked lines. The 2–0 bandhead at 2.29 μm is very weak.

4. Analysis and Results

The iSHELL spectrum exhibits a large number of double-peaked emission lines from rovibrational transitions of CO. The $\upsilon = 1$–0 CO lines up to rotational level $P(47)$ and higher vibrational levels up to $\upsilon = 5$–4 are clearly seen. Emission from ^{13}CO is also seen, in both the $\upsilon = 1$–0 and $\upsilon = 2$–1 transitions. The profiles of the lowest rotational transitions exhibit strong narrow absorption lines, due to absorption from a cold foreground cloud, which cuts out a substantial fraction of the emission. Three H lines (Pfβ, Huϵ, and Huδ) are also seen in emission. The *K*-band iSHELL spectrum also shows a large number of double-peaked lines, all from CO overtone bandhead emission; see Figure 1.

It is clear that the double-peaked ^{12}CO profiles must originate in a rotating accretion disk. To enable a better comparison between ^{12}CO and ^{13}CO lines, we generated median line profiles of the ^{12}CO $\upsilon = 1$–0 and ^{13}CO 1–0 emission lines and also for the ^{12}CO 2–1 and ^{12}CO 2–0 emission lines from the spectrum after subtracting a low-order polynomial continuum. Since we see no difference between low- and high-*J* lines, we created median line profiles of all unaffected by absorption or blending. For the ^{12}CO 1–0 we used $R(14)$, $R(9)$, $R(6)$, $P(8)$, $P(9)$, $P(12)$, $P(14)$, $P(26)$, $P(34)$, $P(37)$, $P(38)$, $P(45)$, and $P(47)$. For ^{13}CO 1–0 we used $R(29)$, $R(24)$, $R(22)$, $R(21)$, $R(19)$, $R(16)$, $R(15)$, $R(13)$, $R(12)$, $R(10)$, $R(9)$, $R(3)$, $P(3)$, $P(7)$, $P(9)$, $P(11)$, $P(12)$, $P(16)$, $P(17)$, and $P(21)$. The ^{12}CO 2–1 transitions were $R(27)$, $R(21)$, $R(20)$, $R(17)$, $R(14)$, $R(13)$, $R(12)$, $R(9)$, $R(1)$, $P(1)$, $P(2)$, $P(6)$, $P(8)$, $P(15)$, $P(21)$, $P(25)$, $P(26)$, $P(28)$, $P(32)$, and $P(33)$, while the transitions for ^{12}CO 2–0 were $R(6)$, $R(7)$, $R(11)$, $R(12)$, $R(14)$, $R(17)$, $R(18)$, $R(20)$, $R(21)$, $R(22)$, $R(23)$, and $R(24)$. These were reinterpolated and centered at the theoretical line center; see Figure 2. From this plot it is easy to see that the ^{13}CO 1 –0 lines are broader and the flanks of the ^{13}CO lines also appear somewhat steeper. The ^{12}CO 2–1 lines are also broader than the 1–0 lines. The overtone ^{12}CO 2–0 lines are even broader than any of the rovibrational lines. The separations between the line peaks are also wider for both ^{13}CO 1 –0 and ^{12}CO 2–1 compared to ^{12}CO 1–0 lines, indicating

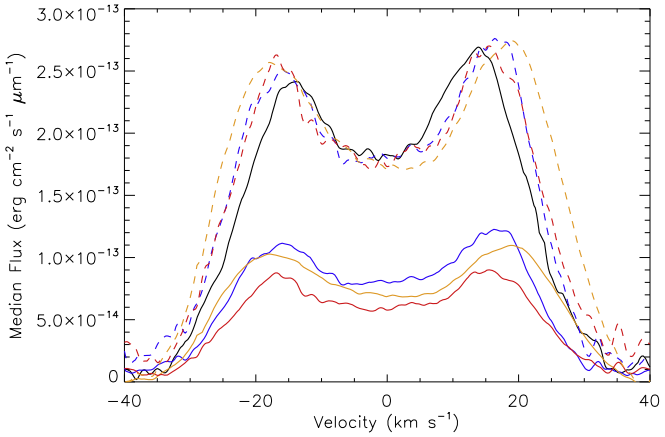

Figure 2. Median line profiles of ^{12}CO $v = 1$–0 and 2–1 and ^{13}CO 1–0 and ^{12}CO 2–0 emission lines. The dashed blue line is the ^{12}CO 2–1 profile scaled by 2.25, the dashed red line is the ^{13}CO 1–0 profile scaled by 3, and the dashed orange line is the scaled ^{12}CO 2–0. The scaled profiles demonstrate the differences in widths compared to the ^{12}CO 1–0 profile.

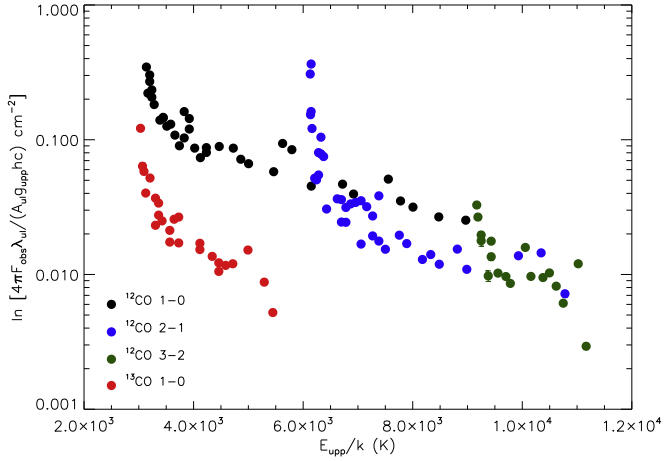

Figure 3. Rotational diagram with the observed data points plotted with large filled circles. The line bands are identified by their colors in the lower left corner of the plot. For almost all of the data, the error bars are smaller than the circle size.

that these lines are inward of the disk relative to the location of the ^{12}CO 1–0 emitting gas. In Table 1 we give the measured FWHMs and peak separations for all the lines shown in Figure 2.

At the 10% level the line widths are similar or $\sim$ 65 km s^{-1}, suggesting that the inner radius is similar for all of them. The FW10% may be slightly larger for the ^{12}CO 2–0 lines. We measure a line width of 68 km s^{-1}. It is not clear whether this difference is real or simply due to measurement inaccuracy, especially since Banzatti et al. (2022) quote an FW10% of 68.9 km s^{-1}. They also quote a slightly larger FWHM of 46.8 km s^{-1}for ^{12}CO 1–0 than what we find, 45.3 km s^{-1}. We determine a $V_{\rm lsr} = +6.7 \pm 2.2$ km s^{-1}for the emission lines. This is a weighted mean of the 2020 September and 2022 April data sets. Banzatti et al. (2022) find a center velocity of $+7$ km s^{-1} (converted to LSR), which agrees very well with what we find.

4.1. Modeling the Emission Lines with a Rotating Keplerian Disk

Inspection of the *K*- and *M*-band spectra yields conflicting information regarding the CO-emitting gas. The relative strengths of the ^{12}CO lines across the *M* band suggest that the gas is optically thick; see the rotational diagram in Figure 3. In addition, the ^{13}CO emission lines are much stronger relative to those of ^{12}CO than expected given the normal isotopic ratio and optically thin gas. However, the clearly double-peaked profiles suggest that the emission cannot be completely optically thick.

In order to determine the properties of the CO-emitting gas, we constructed models of the emission regions under the assumption that the gas was in Keplerian orbit around a 10 $M_\odot$ central source. We considered two configurations: a uniform (i.e., constant temperature and surface density) ring and a thin disk whose temperature and surface density varied with radial distance. We adopted an inclination of 55° derived by Vacca & Sandell (2022). The models assume that the gas is in LTE and are similar to those constructed by Kraus et al. (2000) and others. We generated a synthetic spectrum of the *M*-band emission for each value of temperature between 900 and 2000 K in steps of 100 K and log CO surface density between 15.0 and 22.0 in steps of 0.2. We assumed a source distance of 418 pc and the standard isotopic ratio for ^{12}CO/^{13}CO of 77

Table 1
Line Profile Parameters for Median Averaged Emission Lines

Profile	FWHM (km s^{-1})	Peak Separation (km s^{-1})
^{12}CO $v = 1$–0	45.3	29
^{12}CO $v = 2$–1	48.2	32
^{13}CO $v = 1$–0	48.2	32
^{12}CO $v = 2$–0	54.7	37

Note. The FWHM values have measurement errors of $\sim$ 0.5 km s^{-1}, and the errors for the peak separations are $\sim$ 1 km s^{-1}.

(Wilson & Rood 1994). For the ring models we adopted a radius of 12 au, in order to match the mean width of the emission lines, and a ring width of 1 au. For the disk models we adopted a power-law index of 0.4 for the temperature and 1.5 for the surface density and radial steps of 0.5 au between an inner radius of 5 au and an outer radius of 25 au.

We then reddened each model by $A_V = 8.1$ mag, convolved it with a Gaussian whose width is given by the instrumental resolution ($R \sim 88{,}000$ in the *M* band), and sampled it at the observed wavelength sampling of the observations. A χ^2 comparison between the observed ^{12}CO line spectra and the model spectrum was then computed. For the ring model we computed the best-fit scaling of the model to the spectroscopic data, which corresponds to the best-fit width of the ring. The emission-line strengths were also compared with the values measured from the observed spectra on the standard rotational diagram (Figure 4).

Somewhat surprisingly, we found that no disk models with our assumed parameters were able to provide good matches to the observed spectra. A thin ring model with a temperature of 1500 K and a surface density of $\log N_{\rm CO} = 18.2$ provided a reasonable, although not perfect, fit to the data. It was immediately clear, however, that the ^{13}CO emission was far weaker in the model than in the actual data by a factor of 6–7. This was also reflected in an offset between the points for the ^{13}CO emission-line strengths from the model and those of the data on the rotational diagram, although the slope of the points for the ^{13}CO emission-line strengths from the model matched that of the data (which indicates that the derived temperature

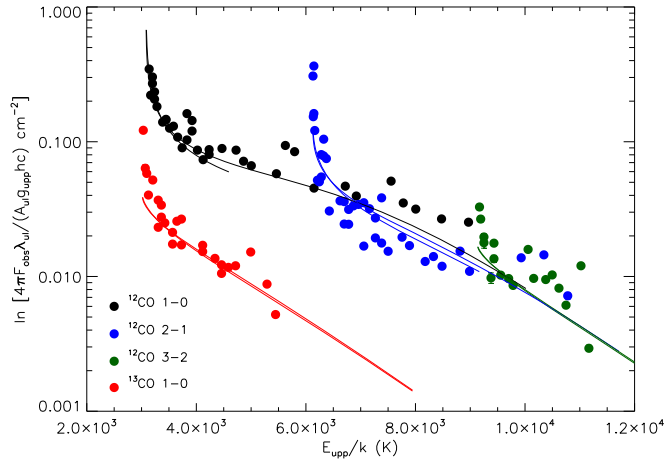

Figure 4. The ring model for a rotational temperature of 1500 K and a density of 1.6×10^{18} cm^{-2} plotted with solid lines on the data points plotted in Figure 3. The model matches the 1–0 data quite well except at the highest energies, where it underestimates the line strength. It also underestimates the line strength at the higher vibrational states, suggesting that the excitation of these lines is dominated by fluorescence. The model overestimates the 2–1 data, most likely because its emitting area is smaller than that of 1–0. The model calculations show that the ^{13}CO abundance needs to be increased by a factor of 6–7 compared to normal interstellar abundances.

was approximately correct). This result, in addition to the differences seen in the line widths of the ^{12}CO and ^{13}CO emission profiles, suggests that the ^{12}CO and ^{13}CO emission arises from different parts of the disk. Therefore, we generated a pure ^{13}CO emission model in which the ^{13}CO gas temperature was the same as that for the ^{12}CO gas, but the abundance was enhanced by a factor of 6, which gave a good fit to the ^{13}CO 1–0 spectra. Figure 5 shows the observed spectra overplotted with the best-fit model without any additional scaling for ^{13}CO. The corresponding line strengths are shown on the rotation diagram in Figure 4.

Despite the excellent agreement between the model and the line strengths seen in Figure 5, it is clear that the best-fit model is somewhat unsatisfactory. A thin ring of CO emission seems physically unrealistic. Furthermore, although the model provides a reasonable match to the overall line strengths, it does not provide a good match to several prominent lines in the spectrum. Many of the ^{12}CO 2–1 lines in the model are much stronger than in the data. In addition, the line profiles of many of the low-lying ^{12}CO 1–0 transitions are not well reproduced by the model.

We have not done a detailed analysis of the *K*-band overtone spectrum, but the 2–0 bandhead emission is very weak and the 3–1 bandhead is almost missing, indicating that the CO gas is quite cold. The best-fit model from the analysis of the rovibrational CO lines provides an adequate fit to the data.

4.2. Absorption Lines

The rovibrational fundamental CO lines in the low *P* and *R* transitions show narrow absorption lines cutting out most of the emission from the accretion disk in the center of the emission lines in the *M*-band spectra. Absorption is also seen in the lowest *R* and *P* transitions of ^{13}CO in both data sets. This suggests that the emission is being absorbed by a cold foreground cloud. This cold foreground cloud is likely to contribute to most of the extinction toward MWC 297, which is estimated to be $\sim$ 8.1 mag (Vacca & Sandell 2022).

The lowest transitions of the CO absorption lines in the 2020 data set are strongly affected by telluric absorption, which makes it difficult to estimate the true extent of the absorption. Therefore, our analysis focused on the 2022 April spectra, for which the relative velocity between the intrinsic absorption and the telluric absorption is larger. In order to extract the absorption lines, we generated a mean profile for the $\upsilon = 1$–0 ^{12}CO emission lines and then scaled that to match the observed profiles of the low-*J* transitions that have the foreground absorption (see Figure 6). Examination of the CO absorption lines indicates that the lowest transitions reach the zero-intensity level and appear much broader than the higher transitions, suggesting that they are optically thick. The higher level *J* transitions agree well in velocity with the ^{13}CO absorption lines, while there is a clear shift in velocity at the lowest levels. We illustrate this in Figure 7, which shows three CO υ 1–0 lines and three of the ^{13}CO lines in the source spectrum, which has been shifted to 0 km s^{-1}. It can be seen from this figure that the weaker absorption lines are blueshifted relative to the disk emission and that the lines are asymmetric, with a red tail (Figure 7). For the optically thin ^{12}CO and ^{13}CO lines we find a velocity of -0.6 ± 0.5 km s^{-1}. With increasing optical depth the blueshift of the lines decreases and the red tail increases. At the lowest *J* levels the CO is very optically thick, the profiles look flat-topped, and the center of the line is shifted to the red. This suggests that there are two absorption components to these lines, with the redshifted component contributing substantially to the width of the lowest and most optically thick transitions. The radial velocity of MWC 297, 6.7 ± 2.2 km s^{-1}, which we determined for the center of the emission lines, is in good agreement with the velocity of the molecular cloud in which it was born. G. Sandell et al. (2023, in preparation) determine a velocity $\sim$ 7.2 km s^{-1}of the molecular cloud from ^{13}CO (6–5) observations with APEX. This agrees well with ^{13}CO (3–2) and C^{18}O (3–2) observations. These lines are unaffected by the cold foreground cloud, while all the emission in the low-*J* ^{12}CO emission is completely absorbed (see also Manoj et al. 2007). Only emission from CO (4–3) and higher rotational levels is unaffected by the cold foreground cloud.

To determine the temperature and column density of the absorbing gas, we performed a curve-of-growth analysis similar to that of Goto et al. (2003). We solved for column density, temperature, and line width using an iterative least-squares fitting routine. However, the low-excitation CO lines are very optically thick and also include the redshifted component, which we cannot separate at the iSHELL resolution. We therefore first analyzed the weaker, and presumably more optically thin, ^{13}CO lines. Using all ^{13}CO lines in the analysis resulted in large densities (2×10^{18} cm^{-2}) and very low temperatures ($\sim$4 K). While these parameters provided a reasonable match to the observed equivalent widths (EWs), the model did not reproduce the line profiles or the depths. The fit is skewed to high densities in order to reproduce the observed EWs, which are clearly dominated by the second red absorption component for the highest optical depth lines. As can be seen in Figure 7, even the ^{13}CO lines exhibit a red wing, which is contributing to the EW. We therefore restricted the EW analysis to the two lowest-opacity lines, for which the red wing appears to have the smallest contribution, and derived a column density of $\sim 6.5 \times 10^{17}$ cm^{-2} and a temperature of $\sim$8.5 K. We then combined the two weakest CO lines with the two weakest ^{13}CO lines in the fit and obtained a solution that matched both the EWs and the line profiles. We kept the velocity width equal to 3.5 km s^{-1}for this fit, which is in agreement with our resolution ($R \sim$ 88,000). This resulted in a CO column density

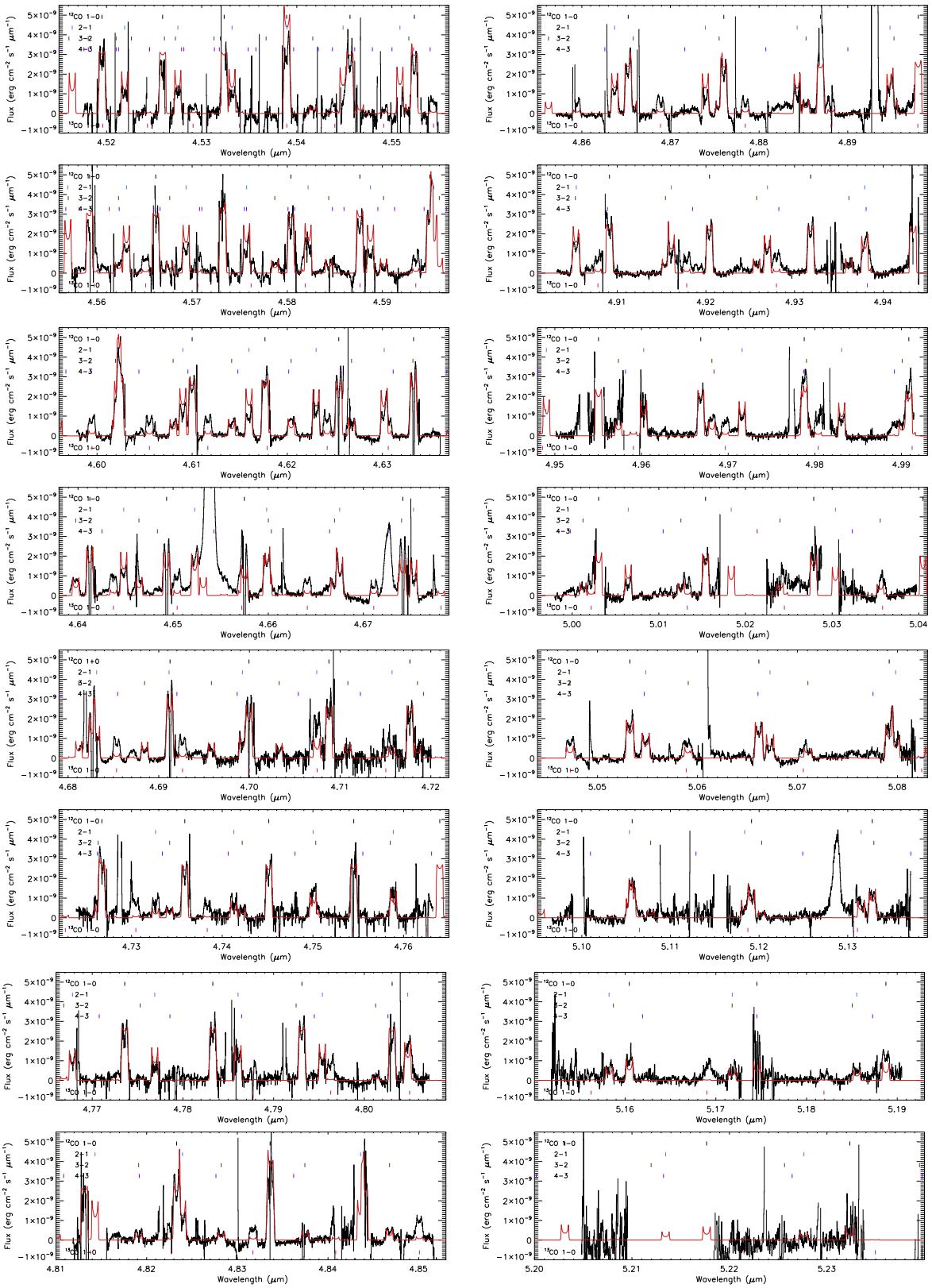

Figure 5. The ring model for $T = 1500$ K and a log density of 18.2 cm^{-2} in red overlaid on the observed *M*-band spectrum. ^{13}CO needs to be scaled by 6 to match the line profiles. The line transitions are marked, and the rovibrational bands they belong to are indicated at the top for ^{12}CO and at the bottom for ^{13}CO 1–0. Regions of strong telluric absorption have been blanked out.

$N(\mathrm{CO}) = (6.7 \pm 0.4) \times 10^{17}$ cm^{-2} and a temperature $T = 8.25 \pm 0.10$ K. Figure 8 shows the ^{12}CO absorption lines with the model fit overlaid in red. No substantial residuals are seen when we subtract this model from the spectrum of the four lines. If we assume a CO abundance of 10^{-4} and that all the hydrogen is molecular and adopt $N(\mathrm{H_2})/A_V = 0.9410^{21}$ molecules cm^{-2}

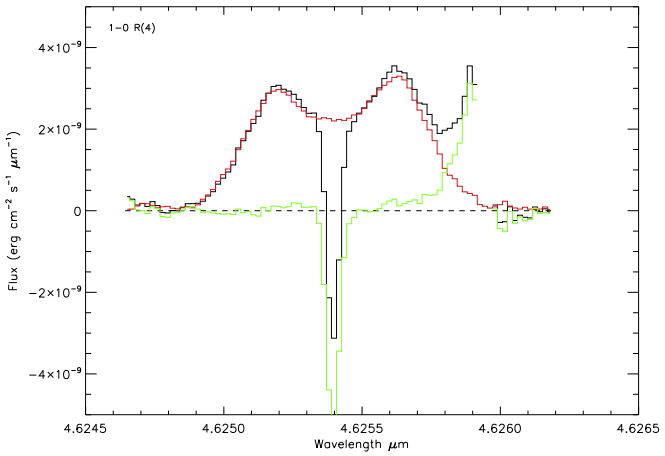

Figure 6. An example illustrating the extraction of absorption-line profiles. The observed emission line, in this case the ^{12}CO $v = 1$–0 $R(4)$, is plotted in black; the scaled template profile is plotted in red; and the resulting absorption profile is plotted in green. The baseline around the absorption profile (green) is quite flat and centered at 0.

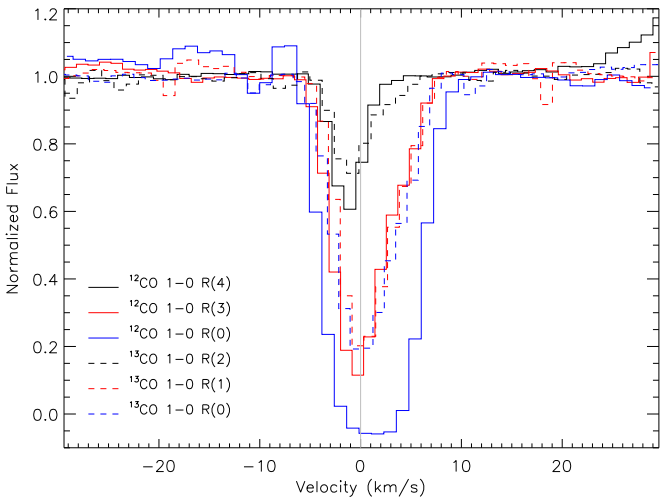

Figure 7. ^{12}CO and ^{13}CO $v = 1$–0 absorption lines. The ^{12}CO and ^{13}CO profiles are plotted with solid and dashed lines, respectively. The lines are identified in the lower left corner of the image. The velocity of the emission lines, centered at 0 km s^{-1}, is marked with a gray vertical line. The optically thick ^{12}CO $v = 1$–0 $R(0)$ line appears flat-topped, much broader, and shifted in velocity relative to ^{12}CO 1–0 $R(4)$ and ^{13}CO 1–0 $R(2)$, which are optically thin. This is because there is a second, colder redshifted cloud component, which is optically thick in the ^{12}CO 1–0 $R(0)$ line. It is also seen in the ^{13}CO 1–0 line as a strong redshifted wing. The 0 km s^{-1}velocity corresponds to a $V_{\rm lsr} = 6.7$ km s^{-1}.

(Bohlin et al. 1978), this absorption component indicates an extinction of 6.3 mag. This, however, is a lower limit to the total foreground extinction since the redshifted absorption component is completely opaque at the lowest CO transitions and also detected in ^{13}CO. It is likely that it is responsible for an additional extinction of 1–2 mag. Therefore, the cold foreground CO emission readily explains the observed foreground extinction of 8.1 mag.

5. Discussion

Generally half of all solar-mass stars have lost their disks after 3 Myr, with an overall disk life time of 6 Myr (Haisch et al. 2001). Some stars still have disks after 10 Myr (see, e.g., Espaillat et al. 2008). However, disk dispersion timescales for high-mass stars are much shorter. By the time O and B stars become optically visible, they have long since dispersed their disks. It is therefore not surprising that hardly any disks have been detected around visible early B stars. The two previously known examples are the early B star MWC 349 A and LkHα 101. The latter is a B1Ve star that illuminates an H II region. Infrared interferometry shows that it is surrounded by an almost face-on disk with an inner hole and a dust radius of $\sim$ 30 au (Tuthill et al. 2002). MWC 297 is now a third example. It has long been suspected to have an accretion disk, but the disk size and inclination have been uncertain. MWC 297 is a much younger star than MWC 349 A or LkHα 101, as it is still heavily accreting with an age in the range of (1–2.8) $\times$ 10^5 yr (Fairlamb et al. 2015; Vioque et al. 2018).

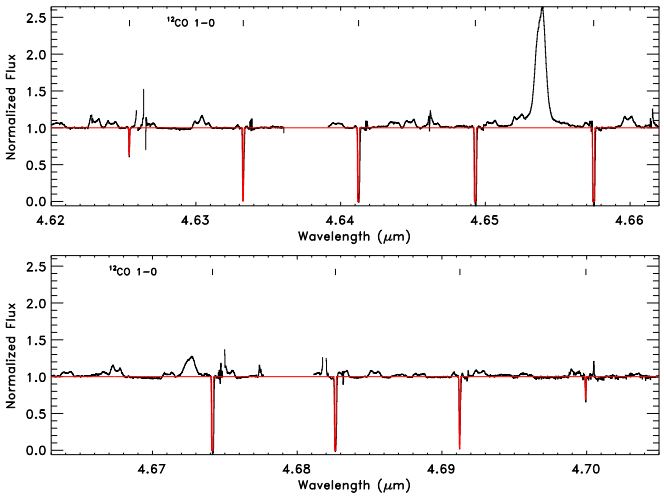

Figure 8. The iSHELL spectrum showing the $v = 1$–0 ^{12}CO lines in absorption. The wavelength region is split into two for clarity. The transitions $R(3)$, $R(2)$, $R(1)$, and R(0) are at the top, and $P(1)$, $P(2)$, $P(3)$, and $P(4)$ are at the bottom, left to right. Regions of strong telluric absorption have been blanked out. The fainter double-peaked emission lines are from higher rotational rotation transitions. The strong hydrogen lines Pfβ and Huϵ are also seen. The model fit to the absorption lines is overlaid in red.

The rovibrational CO lines and the CO overtone bands show clear double-peaked profiles confirming that we see an inclined circumstellar disk around MWC 297, which is in Keplerian rotation. MWC 297 does not really fit in the classification scheme by Meeus et al. (2001) since it is much younger than typical HAeBe stars, but if one follows the Meeus classification, it would be in group I (Guzmán-Días et al. 2021). For this reason Acke & van den Ancker (2004) added a group III for deeply embedded and accretion-dominated HAEBE stars. Neither does MWC 297 readily fit into the classification of CO spectra by Banzatti et al. (2018, 2022) and Bosman et al. (2019). It has double-peaked profiles, and the ratio of vibrational levels of $v2/v1 = 0.45$ puts it in region 1, but since there is no cold dust in the disk (Vacca & Sandell 2022), we cannot definitely say whether it belongs to region 1a or region 1b. However, since the UV fluorescence dominates the excitation of the $v = 2$–1 and 3–2 bands and even appears to dominate the high excitation levels of CO 1–0, it should probably go into group 1b. We also note there are only five HAeBe stars that have overtone bandhead CO emission (Banzatti et al. 2022), yet the bandhead emission was easily detected in MWC 297. Usually the overtone emission comes from hot, dense CO gas in the innermost part of the disk (Ilee et al. 2013, 2014) with gas temperatures of $\sim$3000 K and column densities of 10^{21} cm^{-2}. The overtone emission in

MWC 297 is much colder, ~1500 K, an order of magnitude less dense, and extending up to a radius of 10 au.

It was clear from the modeling of the CO 1–0 lines that the line strengths cannot be fit with a single-temperature model. There is very little change in line strength between low- and high-excitation lines, and they all have the characteristic double-peaked profile from a disk in Keplerian rotation. An isothermal fit to all the rotational lines results in very high optical depths for the lowest transition and makes the line profiles flat-topped, which is not what is observed. It is clear that the lines can only be moderately optically thick, since they all show a clear U-shaped profile. Neither can a single-temperature model explain the strong $\upsilon = 2$–1 and 3–2 transitions, which for the 2–1 lines are almost half the line strengths of the 1–0 lines. This was already noticed by Brittain et al. (2003), who argued that the strong $\upsilon = 2$–1 and 3–2 transitions in isolated HAeBe star HD 141569 must be excited by UV fluorescence; see also Brittain et al. (2007). Recent modeling of HD 141569, which is a well-studied HAeBe star with vibrational levels detected up to $\upsilon = 7$–6, confirms that fluorescence is needed to explain the observed rovibrational lines (Jensen et al. 2021). We expect MWC 297 to have strong UV radiation, both from the fact that it is an early B star and because it is heavily accreting. However, due to the high foreground extinction, 8 .1 mag, the star is not visible in the UV. Therefore, we have not attempted to include fluorescence in our model, although it it is clear that UV fluorescence is needed to explain the emission in the higher vibrational bands and even necessary for the high-excitation 1–0 lines. The same may be true for other HAeBe disks as well.

Because MWC 297 is very bright in the infrared, it has been the target of many interferometric studies. These studies show a well-resolved inner disk in the continuum with a size of 2–4 au in continuum (Malbet et al. 2007; Kraus et al. 2008; Acke et al. 2008; Weigelt et al. 2011; Hone et al. 2017; Kluska et al. 2020), with the line emission (Brγ) being 2–3 times more extended (Malbet et al. 2007; Kraus et al. 2008; Weigelt et al. 2011; Hone et al. 2017). Acke et al. (2008) also observed MWC 297 in the mid-infrared. Modeling of mid-infrared data required a two-component model, and they found a smaller inner disk with a size of 4 au and a more extended disk with a size of 17 au (40 mas). This is rather similar to the size of the disk we see in CO. Neither do these studies find any inner gap (Acke et al. 2008; Kluska et al. 2020). What is also noteworthy is that the size of the continuum region is well within the dust destruction radius, which for MWC 297 is ~5 au.[4] As pointed out by Vacca & Sandell (2022), the Brγ emission is extremely optically thick, and it therefore appears that the continuum comes from an optically thick gaseous region. From the observed line width of the CO lines at 10% level, ~65.2 km s^{-1}, we find the inner CO radius ~5.6 au, i.e., roughly at the same radius as the dust destruction radius.

A normal isotope ratio of [^{12}C/^{13}C] of 77 greatly underestimates the strength of the observed ^{13}CO line intensities. We find that a relative ^{12}CO-to-^{13}CO abundance ratio of ~6 provides a good fit to the data. This does not mean that the disk has anomalous isotope ratios, but rather that ^{13}CO is not in LTE and coexisting with ^{12}CO. As was seen, the FWHM of ^{13}CO 1–0 differs by more than 5% from that of 1–0; see Section 4. These kinds of ^{12}CO/^{13}CO ratios are not uncommon. Van der Plas et al. (2015) found that the ^{12}CO/^{13}CO ratio varied between 3 and 7 for their sample of 12 HAeBe stars and that the rotational temperatures of ^{13}CO were on average lower than those for ^{12}CO. Banzatti et al. (2022), who have the largest sample of rovibrational CO lines in HAeBe stars, do not quote a ^{12}CO/^{13}CO ratio, but looking at the line ratios for their sample of 17 HAeBe stars with double-peaked line profiles shows that the ratio ranges from 3 to 25, with a median of 14. This does not directly translate to an abundance ratio [^{12}CO/^{13}CO], because for most disks ^{12}CO 1–0 is more optically thick than ^{13}CO 1 –0, nor does it account for the difference in excitation between ^{12}CO and ^{13}CO.

We detect narrow absorption lines, FWHM ~ 4–5 km s^{-1}, from a cold unrelated foreground cloud in both ^{12}CO and ^{13}CO. Radio observations show that this foreground cloud is very extended and therefore more local, probably somewhere around 100–200 pc from us. At the lowest-J transitions the absorption lines in ^{12}CO are completely saturated. At higher J levels the lines become more blueshifted and agree in velocity with the ^{13}CO absorption lines. The lowest transitions of ^{13}CO are also optically thick and show a redshifted line wing. Detailed analysis shows that the redshifted component comes from a colder but less dense cloud component. For the blueshifted cloud component, which is at a $V_{\rm lsr} \sim 6.4$ km s^{-1}, we derive a temperature of 8.3 ± 0.1 K and a CO column density $N({\rm CO}) = 6.7 \times 10^{17}$ cm^{-2}. If we assume that all the CO gas is molecular with a typical abundance ratio of 10^{-4}, it corresponds to an extinction of 6.3 mag assuming the standard relation between molecular hydrogen and extinction. Since the redshifted cloud component also contributes to the extinction, it is clear that a foreground cloud plus diffuse gas along the line of sight can fully explain the observed high extinction, 8.1 mag, toward MWC 297. Banzatti et al. (2022) noticed that the absorption-line FWHM decreased as a function of J level from 10 km s^{-1} in the $J = 1$ lines down to a minimum of 3.3 km s^{-1}in the $\upsilon = 1$–0 $J = 4$ lines and that the line shape also changed, becoming less Gaussian and showing effects of saturation at the lowest J levels. They also saw a similar behavior in ^{13}CO. This agrees well with what we have found, and we now know that it is due to two cold clouds in the foreground of MWC 297 with different temperatures and densities, but both of these are completely optically thick in ^{12}CO at the lowest J levels.

6. Summary and Conclusions

We have shown that overtone bandhead and rovibrational CO lines trace a hot gas disk in Keplerian rotation around the 10 $M_\odot$ star MWC 297. Our modeling shows that the emission cannot be explained by thermal excitation alone. It therefore appears that the high-excitation rotational lines are largely excited by fluorescence, something that has been seen in other HAeBe disks as well. Analysis of the spectra shows that ^{12}CO $\upsilon = 1$–0 emission is optically thick for the low-excitation lines. Even ^{13}CO 1–0 and ^{12}CO 2–1 have somewhat optically thick lines at low J levels. We find that a narrow ring with a radius of 12 au and an inclination of 55° provides an adequate fit to the data. For this model we derive a rotational temperature of 1500 K and a CO column density of 1.6×10^{18} cm^{-2}. This model underestimates the line strength of high-J lines, indicating that these lines are excited by fluorescence. The CO overtone emission, which is only seen in a few HAeBe

[4] Kluska et al. (2020) quote a dust destruction radius of 8 au, but that is because they use a stellar luminosity of 4×10^4 $L_\odot$, which is far too high for a B1.5V star; see Vacca & Sandell (2022).

disks, has a similar temperature. Our best-fit model is still somewhat unsatisfactory. A thin ring of CO emission seems physically unrealistic. Furthermore, although the model provides a reasonable match to the overall line strengths, it does not provide a good match to several prominent lines in the spectrum. Many of the ^{12}CO 2–1 lines in the model are much stronger than in the data. We also find that a normal isotope ratio of [^{12}C/^{13}C] of 77 greatly underestimates the ^{13}CO line intensities, while a ^{12}CO-to-^{13}CO abundance ratio of $\sim$ 13 provides a good fit to the data. Other HAeBe disks typically show similarly enhanced ^{13}CO line intensities, most likely because excitation conditions in the disks differ between ^{12}CO and ^{13}CO.

The ^{12}CO 1–0 spectrum shows a strong absorption feature in the center of the emission profile, which is completely saturated at $J = 1$ and 2, and which is also seen in ^{13}CO 1–0. This absorption is due to cold foreground emission, which is unrelated to MWC 297. Radio observations show that this foreground cloud is very extended and therefore more local, probably somewhere around 100–200 pc from us. Detailed analysis shows that this foreground absorption is caused by two cold foreground clouds, partly overlapping in velocity. The more opaque one is slightly blueshifted relative to the center of the emission lines and has a temperature of 8.3 K and a column density of 6.7×10^{17} cm^{-2}, which correspond to a visual extinction of 6.3 mag. With our velocity resolution we could not separate the second redshifted component well enough to be able to get a good estimate the temperature and density, but it is apparent that it is colder and has a lower column density. It is clear that these foreground clouds are responsible for the high extinction toward MWC 297.

We have shown that the young, heavily accreting B1.5V star MWC 297 is still surrounded by a molecular accretion disk in Keplerian rotation. It is the only early B star that has been detected in rovibrational CO lines and one of the few HAeBe stars detected in overtone CO emission. The circumstellar disk has not been detected at millimeter wavelengths, because a cold foreground cloud absorbs all the low-J ^{12}CO lines. These lines are typically used for detecting gas in disks with facilities like SMA and ALMA. The MWC 297 disk does not have any cold dust. In that sense it resembles MWC 349A, which has been detected in CO overtone emission but has not been detected in any molecular line at millimeter wavelengths, suggesting that it has no cold molecular gas. For the same reason we find it very unlikely that MWC 297 would have any cold molecular gas. Based on the rovibrational lines, it also looks like the disk is rather compact. It would be very interesting to get a better estimate of the size of the disk using spectroastrometric imaging using the rovibrational CO lines.

Acknowledgments

We appreciate Prof. Andrea Banzatti sharing some of his iSHELL data on MWC 297 with us. We also thank Dr. Adwin Boogert for helping us with the telluric correction of the 2020 September iSHELL spectrum. We are especially grateful to the anonymous referee, whose constructive criticism encouraged us to completely rethink our modeling approach to the CO lines and to get additional data.

ORCID iDs

Göran Sandell https://orcid.org/0000-0003-0121-8194
William Vacca https://orcid.org/0000-0002-9123-0068

References

Acke, B., & van den Ancker, M. E. 2004, A&A, 426, 151
Acke, B., Verhoelst, T., van den Ancker, M. E., et al. 2008, A&A, 485, 209
Banzatti, A., Abernathy, K. M., Brittain, S., et al. 2022, AJ, 163, 174
Banzatti, A., Garufi, A., Kama, M., et al. 2018, A&A, 609, L2
Banzatti, A., & Pontoppidan, K. M. 2015, ApJ, 809, 167
Bast, J. E., Brown, J. M., Herczeg, G. J., et al. 2011, A&A, 527, A119
Beltrán, M. T., & de Wit, W. J. 2016, A&ARv, 24, 6
Bik, A., Kaper, L., & Waters, L. B. F. M. 2006, A&A, 455, 561
Bik, A., & Thi, W. F. 2004, A&A, 427, L13
Blake, G. A., & Boogert, A. C. A. 2004, ApJL, 606, L73
Blum, R. D., Barbosa, C. L., Damineli, A., et al. 2004, ApJ, 617, 1167
Bohlin, R. C., Savage, B. D., & Drake, J. F. 1978, ApJ, 224, 132
Bosman, A. D., Banzatti, A., Bruderer, S., et al. 2019, A&A, 631, A133
Brittain, S. D., Carr, J. S., & Najita, J. R. 2018, PASP, 130, 074505
Brittain, S. D., Rettig, T. W., Simon, T., et al. 2003, ApJ, 588, 535
Brittain, S. D., Simon, T., Najita, J. R., et al. 2007, ApJ, 659, 685
Brown, J. M., Pontoppidan, K. M., van Dishoeck, E. F., et al. 2013, ApJ, 770, 94
Cooper, H. D. B., Lumsden, S. L., Oudmaijer, A. D., et al. 2013, MNRAS, 430, 1125
Cushing, M. C., Vacca, W. D., & Rayner, J. T. 2004, PASP, 116, 362
Doppmann, G. W., Najita, J. R., & Carr, J. S. 2017, ApJ, 836, 242
Drew, J. E., Busfield, G., Hoare, M. G., et al. 1997, MNRAS, 286, 538
Espaillat, C., Muzerolle, J., Hernández, J., et al. 2008, ApJL, 689, L145
Fairlamb, J. A., Oudmaijer, R. D., Mendigutía, I., et al. 2015, MNRAS, 453, 976
Goto, M., Usuda, T., Takato, N., et al. 2003, ApJ, 598, 1038
Guzmán-Días, J., Medigutía, I., Montesinos, B., et al. 2021, A&A, 650, A182
Haisch, K. E., Lada, E. A., & Lada, C. J. 2001, ApJL, 533, L153
Herczeg, G. J., Borwn, J. M., van Dishoeck, E. F., et al. 2011, A&A, 533, A112
Hone, E., Kraus, S., Kreplin, A., et al. 2017, A&A, 609, A17
Ilee, J. D., Fairlamb, J., Oudmaijer, R. D., et al. 2014, MNRAS, 445, 3723
Ilee, J. D., Oudmaijer, R. D., Wheelright, H. E., et al. 2018, MNRAS, 477, 3360
Ilee, J. D., Wheelright, H. E., Oudmaijer, R. D., et al. 2013, MNRAS, 429, 2960
Ishii, M., Nagata, T., Sato, S., et al. 2001, AJ, 121, 3191
Jensen Jr., S. K., Brittain, S. D., Najita, J. R., et al. 2021, PASP, 133, 104402
Kluska, J., Berger, J.-P., Malbet, F., et al. 2020, A&A, 636, A116
Kraus, M., Arias, M. L., CZidale, L. S., et al. 2020, MNRAS, 493, 4308
Kraus, M., Hofmann, K.-H., Benisty, M., et al. 2008, A&A, 489, 1173
Kraus, M., Krügel, E., Thum, C., et al. 2000, A&A, 362, 158
Lazareff, B., Berger, J.-P., Kluska, J., et al. 2017, A&A, 599, A85
Malbet, F., Benisty, M., de Wit, W.-J., et al. 2007, A&A, 464, 43
Manoj, P., Ho, P. T. P., Ohashi, N., et al. 2007, ApJL, 667, L187
Meeus, G., Waters, L. B. F. M., Bouwman, J., et al. 2001, A&A, 365, 476
Moscadelli, L., Cesaroni, R., Beltrán, M. T., et al. 2021, A&A, 650, A142
Najita, J., Carr, J. S., & Mathieu, R. D. 2003, ApJ, 589, 931
Najita, J. R., Carr, J. S., Glassgold, A. E., et al. 2007, in Protostars and Planets V, ed. B. Reipurth, D. Jewitt, & K. Keil (Tucson, AZ: Univ. of Arizona), 507
Navarete, F., Damineli, A., Steiner, J. E., et al. 2021, MNRAS, 503, 270
Pomohaci, R., Oudmaijer, A. D., Lumsden, S. L., et al. 2017, MNRAS, 472, 3624
Pontoppidan, K. L., Blake, G. A., & Smette, A. 2011, ApJ, 733, 84
Rayner, J., Tokunaga, A., Jaffe, D., et al. 2022, PASP, 134, 015002
Riello, M., De Angelim, F., Evans, D. W., et al. 2021, A&A, 649, A3
Salyk, C., Blake, G. A., Boogert, A. C. A., et al. 2009, ApJ, 699, 330
Sandell, G., Weintraub, D. A., & Hamidouche, M. 2011, ApJ, 727, 26
Sandell, G., Wright, M., Güsten, R., et al. 2020, ApJ, 904, 139
Scoville, N. Z., Hall, D. N. B., Kleinmann, S. G., et al. 1979, ApJL, 232, L121
Scoville, N. Z., Kleinmann, S. G., Hall, D. N. B., et al. 1983, ApJ, 275, 201
Tuthill, P. G., Monnier, J. D., Danchi, W. C., et al. 2002, ApJ, 577, 826
Vacca, W. D., Cushing, M. C., & Rayner, J. T. 2003, PASP, 115, 389
Vacca, W. D., & Sandell, G. 2022, ApJ, 941, 189
van der Plas, G., van der Ancker, M. E., Waters, L. B. F. M., et al. 2015, A&A, 574, A75
Vioque, M., Oudmaijer, R. D., Baines, D., et al. 2018, A&A, 620, A128
Weigelt, G., Grinin, V. P., Groh, J. H., et al. 2011, A&A, 527, A103
Wheelwright, H. E., Oudmaijer, R. D., de Wit, W. J., et al. 2010, MNRAS, 408, 1840
Williams, J. P., & Cieza, L. A. 2011, ARA&A, 49, 67
Wilson, T. L., & Rood, R. T. 1994, ARA&A, 32, 191
Zapata, L. A., Garay, G., Palau, A., et al. 2019, ApJ, 872, 176